Sensitive and Ultrabroadband Phototransistors Based on 2D Bi₂O₂Se Nanosheets with Spectral Response

Tong Tong, Yunfeng Chen, Shuchao Qin, Weisheng Li, Junran Zhang, Chunchen Zhang, Xiao Yuan, Xiaoqing Chen, Luo Man, Xinran Wang, Weida Hu*, Fengqiu Wang*, Wenqing Liu, Peng Wang, Xuefeng Wang*, Rong Zhang* and Yongbing Xu*

T. Tong, S. C. Qin, W. S. Li, J. R. Zhang, X. Yuan, X. Q. Chen, Prof. X. R. Wang, Prof. F. Q. Wang, Prof. X. F. Wang, Prof. R. Zhang and Prof. Y. B. Xu
National Laboratory of Solid State Microstructures and Jiangsu Provincial Key Laboratory of Advanced Photonic and Electronic Materials, School of Electronic Science and Engineering, Nanjing University, Nanjing 210023, China
E-mail: ybxu@nju.edu.cn; fwang@nju.edu.cn; xfwang@nju.edu.cn; rzhang@nju.edu.cn

Y. F. Chen and Prof. W. D. Hu
State Key Laboratory of Infrared Physics, Shanghai Institute of Technical Physics, Chinese Academy of Sciences, 500 Yu tian Road, Shanghai 200083, China
E-mail: wdhu@mail.sitp.ac.cn

C. C. Zhang and Prof. P. Wang,
National Laboratory of Solid State Microstructures, College of Engineering and Applied Sciences and Collaborative Innovation Center of Advanced Microstructures, Nanjing University, Nanjing 210023, China

Prof. W. Q. Liu
Department of Electronic Engineering, Royal Holloway, University of London, Egham, Surrey TW20 0EX, UK

Prof. Y. B. Xu
York-Nanjing Joint Center in Spintronics, Department of Electronic Engineering and Department of Physics, The University of York, York YO10 5DD, UK

T. Tong, Y. F. Chen and S. C. Qin contributed equally to this work.

Abstract:

Bi$_2$O$_2$Se, a high-mobility and air-stable 2D material, has attracted great attention in integrated logic electronics and optoelectronics. However, it remains a challenge to achieve the overall high-performance in a wide spectral range for Bi$_2$O$_2$Se based devices. Here, a broadband phototransistor with high photoresponsivity is reported by employing the high-quality large area (~180 μm) Bi$_2$O$_2$Se nanosheets synthesized via a modified chemical vapor deposition (CVD) method with the face-down configuration. The device covers ultraviolet (UV)-visible (Vis)-near infrared (NIR) wavelength range (360 ~1800 nm) at room temperature, exhibiting a maximum responsivity of 108696 A/W at 360 nm, which is a record among currently reported 2D semiconductors and two orders of magnitude higher than that of other CVD-grown 2D materials. Upon 405 nm illumination, the external quantum efficiency (*EQE*), photoresponsivity (*R*) and specific detectivity (*D**) of the device can reach up to 1.5×10^7 %, 50055 A/W and 8.2×10^{12} Jones respectively, which is attributable to a combination of the photogating, photovoltaic and photothermal effects. Our devices reach a -3 dB bandwidth of 8 kHz, accounting for a fast rising time of 32 μs. High responsivity, fast response time and environmental stability achieved simultaneously in the 2D Bi$_2$O$_2$Se phototransistors make such an approach of practical relevance. This work demonstrates that Bi$_2$O$_2$Se phototransistors, developed from the improved CVD growth, with outstanding photoelectric properties, can realize in high-quality ultraviolet and infrared imaging application.(Bi$_2$O$_2$Se 可以在紫外和红外波段成像，文中成像图 6）as previous

1. Introduction

Photoransistors with a broad spectral response range covering the UV-Vis-NIR (360 ~1800 nm) have attracted great attention in a variety of telecommunications and photoelectric applications.[1-3] Currently, a large number of phototransistors based on 2D materials such as graphene,[4,5] transition metal dichalcogenides (TMDs),[6-8] black phosphorous (BP)[9-10] and InSe[11], have been demonstrated. Graphene has a strong interaction with photons in a very wide spectral range because of its gapless nature.[12] However, the relatively low absorbance (~ 2.3 %) of a single layer carbon atoms adversely limits its photoresponsivity.[12] The TMDs such as MoS_2 exhibits excellent photoresponsivity but its response speed is slow.[13-15] Most MoS_2-based devices only operate in a narrow visible spectral range due to its large bandgaps.[15] BP[16] and InSe[11] show outstanding broadband photoelectric properties, but the instability at ambient environment has hindered their potential for broadband application.[17] Ideal phototransistors should have fast respond, high sensitivity in a wide spectral range and air-stability, which are rare to implement in 2D materials.

Layered Bi_2Se_3 is a typical topological insulator with an insulating bulk gap and conductive surface states.[18] A ternary compound of Bi_2O_2Se with substituting O atoms for Se atoms in Bi_2Se_3 possesses a tetragonal structure.[19] More recently, the air-stable layered Bi_2O_2Se has emerged as a promising new 2D semiconductor with excellent properties.[20-22] Through magnetic transport measurement, it was found that the 2D Bi_2O_2Se shows strong spin-orbit interaction,[23] and at the same time maintains the high mobility of ~28900 $cm^2V^{-1}s^{-1}$ at 2 K.[24] The Bi_2O_2Se based field-effect transistor also demonstrate superior current on/off ratio of > 10^6 with almost ideal

subthreshold swing (~ 65 mV/dec), which is significant for low-power logic devices.[19] Furthermore, Bi_2O_2Se possesses a moderate band gap (~0.8 eV),[24] which leads to its device suitable for photodetection in a wide spectral range. The ultrahigh mobility, superior air-stability and moderate bandgap make Bi_2O_2Se a promising semiconductor candidate for photoelectric applications.

Here, we synthesized high-quality large area (~180 μm) Bi_2O_2Se nanosheets of about 10 nm in thickness through the modified chemical vapor deposition (CVD) method with the face-down configuration. Bi_2O_2Se phototransistors by employing Al_2O_3 (30 nm) as dielectric layer are successfully implemented. The photodetection wavelength of the device covers UV-Vis-NIR range and the photoresponsivity reaches up to 108696 A/W (360 nm), 50055 A/W (405 nm), 25505 A/W (532 nm), 843.5 A/W (808 nm), 118 A/W (1310 nm) and 22.12 A/W (1550 nm), respectively. Upon 405 nm illumination, the *EQE* and response time can approach up to 1.5×10^7 % and 32 μs, respectively, the highest and fastest among the 2D material based phototransistors reported so far.[11-16] The mechanism of the high responsivity in a wide spectral range (360 ~1800 nm) can be further explained by the photogating, photovoltaic and photothermal effects. Bi_2O_2Se phototransistors are demonstrated to be crucial for the applications in the integrated circuits.

2. Result and Discussion

There are two possible channels for the CVD growth of the Bi_2O_2Se nanosheets with the face-down configuration**:** (1) Bi_2O_3 powder adsorb and diffuse on the substrate, reacting with Bi_2Se_3 to form Bi_2O_2Se. (2) Bi_2O_3 and Bi_2Se_3 react directly in the gas phase and the resulting Bi_2O_2Se clusters adsorb, nucleate and grow on the

substrate. Clearly, these two channels all involve multiple elementary process. Although the growth dynamics of Bi_2O_3 and Bi_2Se_3 are still not fully understood, the first channel may provide better local environment for the high-quality growth as designed in our experimental configuration. The schematic drawing of the CVD system processing a single temperature zone is presented in **Figure 1**a. Briefly, Bi_2Se_3 powder and Bi_2O_3 powder are put in two quartz boats at the hot center as evaporation sources respectively. The distance between the two quartz boats is 8 cm, which is to ensure that the Bi_2Se_3 vapor concentration gradient on the mica substrate can be ignored, compared with the Bi_2O_3 density, as required for the first channel growth mode. Fluorophlogopite mica ($KMg_3AlSi_3O_{10}F_2$) is considered to be an excellent van der Waals (vdW) epitaxy substrate for growing 2D material, due to its flatness, surface inertness and rather high thermal stability.[25,26] The chemically inert substrate can circumvent strict requirement of lattice matching, facilitating the epitaxial growth of Bi_2O_2Se nanosheets.[27, 28] Herein, the freshly cleaved fluorophlogopite mica is utilized as growth substrate, which is mounted on the top of the quartz boat, facing down to the Bi_2O_3 power (see the Experimental Section for details). Under this circumstance, the density of the precursor (Bi_2O_3) is relatively high. During the Bi_2O_2Se growth, Bi_2O_3 in the vapor phase undergoes a two-step reaction, where Bi_2O_{3-x} is likely formed during the reaction as an intermediate phase and these suboxide compounds diffuse to the mica and further react with the Bi_2Se_3 vapor to grow Bi_2O_2Se nanosheets. As that observed in MoS_2,[29, 30] the large density of

nucleation sites, acting as the seeds, is expected to promote the large areas of high quality layer growth of the Bi_2O_2Se nanosheets with the face-down configuration.

Figure 1b shows a typical optical microscopy of the Bi_2O_2Se nanosheet grown on mica substrate. It is clearly seen that the Bi_2O_2Se nanosheet exhibits the square or rectangular shape with a large average domain size of ~180 μm. Atomic force microscope (AFM) in **Figure 1**c shows that the thickness of Bi_2O_2Se is about 9.8 nm and the root-mean-square (RMS) roughness is only 70 pm, indicating the sample with the atomic scale flatness. To further evaluate the crystal structure and chemical compositions of as-grown Bi_2O_2Se nanosheets, high-angle annual dark-field (HAADF) imaging and energy-dispersive X-ray spectroscopy (EDS) mapping are conducted on an aberration-corrected scanning transmission electron microscope (STEM) system. The as-grown Bi_2O_2Se nanosheets can be transferred onto the holey carbon-supported Cu grid for STEM characterization by a poly (methyl methacrylate) PMMA-mediated method (See the Experimental Section for details).[31] HAADF-STEM image of square atom lattice are described in **Figure 1**d and the corresponding fast Fourier transform (FFT) illustrated in the inset of **Figure 1**d, conforming the tetragonally arranged atoms. The square spots (200) and (105) agree well with the single-crystal Bi_2O_2Se of I4/mmm space group.[24] **Figure 1**e-h illustrate the EDS element mapping of Bi_2O_2Se nanosheets and corresponding elemental maps for Bi (f), O (g), Se (h) and selected region (e), showing uniform distribution of three elements. The Raman spectrum of Bi_2O_2Se is shown in Figure S1 (Supporting Information). Two peaks are located at 100 cm^{-1} and 159 cm^{-1}, associated with the E_g^2 and A_{1g}^2 phonon modes,

respectively. These spectroscopic characterizations show that the as-grown Bi_2O_2Se nanosheets are of high quality, which are prerequisite for high performance photoelectric devices.

To investigate the photoelectric properties of the Bi_2O_2Se nanosheets, we fabricated top-gate Bi_2O_2Se phototransistors on the mica substrate employing Al_2O_3 (30 nm) as dielectric layer (more experimental details are described in the Experimental Section), in which the Bi_2O_2Se flakes are about 10 nm. The schematic view of the Bi_2O_2Se phototransistor is shown in **Figure 2**a. In **Figure 2**b, the transfer curve of the phototransistor with different incident laser power density ranging from 5.11 to 31.4 nW (V_{ds} = 2 V) for 405 nm illumination are studied at 300 K. The transfer curve shows a negative-shift, which is consistent with the photogating effect.[32, 33] It is clear that the photocurrent ($I_{ph} = I_{illuminated} - I_{dark}$) increases with the laser power and gate bias. Upon 405 nm illumination, a significant increasement of photocurrent I_{ph} at a fixed gate bias is observed, showing a strong dependence on laser power, which is resulted from more photogenerated carriers generation under high laser intensity.[34] With increasing the positive voltage, the Fermi level of Bi_2O_2Se is moving closer to its conduction band, so that the barrier height between the Bi_2O_2Se and electrodes can be lowered, which increases the tunneling and thermal current.[35] Furthermore, when the temperature decreases to 110 K, the Bi_2O_2Se phototransistor reaches to a large on/off ratio of ~10^7 (Figure S2, Supporting Information). Moreover, the photocurrent I_{ph} also increases with the increasing of V_{ds} (Figure S3, Supporting Information), owing to the enhancement of carrier drift-velocity.[36,37]

Photoresponsivity (R), the external quantum efficiency (EQE) and the detectivity (D^*) are the significant figure-of-merit for phototransistors. They are calculated by following equations

$$R(A/W) = I_{ph}\big/P_{opt} \tag{1}$$

$$EQE = \frac{hcR}{e\lambda} \tag{2}$$

$$D^* = (A\Delta f)^{\frac{1}{2}}\big/NEP \tag{3}$$

where I_{ph} is the photocurrent, P_{opt} is the illumination power irradiated onto the channel, A is the effective area, h is Planck's constant, c is the velocity of light, e is the electronic charge, λ is the wavelength of the incident power, R is the responsivity, Δf is the electrical bandwidth in Hz, and NEP is the noise equivalent power.[38] The photoresponsivity and photocurrent measured at $V_{ds} = 2$ V, $V_G = 12$ V are summarized in **Figure 2**c. It is clear that the photocurrent increase with increasing laser power, and the R of our device can reach ~ 50055 A/W under the low light intensity (405 nm, 5.11 nW), which is one of highest values of reported 2D semiconductors.[33, 38, 39] The high photoresponsivity can be attributed to the photogating effect, which will be discussed in detail later. A sub-linear dependence of the photoresponse is observed upon changing the light power.[40] The saturated absorption and the screening effect[40] at higher laser level are responsible for the decreased photoresponsivity. With increasing power, the available trap states in the Bi_2O_2Se would be filled, which also reduce gain and photoresponsivity (to be discussed in later section). EQE is another important parameter to reflect the ratio of electron flowing out of the device in

response to impinging photons. The maximum of *EQE* can reach ~1.53×10^7 % in **Figure 2**d, which is higher than other 2D materials, such as HfS_2[41] and InSe[42]. The other criterion is specific detectivity (*D**), reflecting the phototransistor's sensitivity. When assuming that the dark current is the major contribution to the shot noise, *D** can be expressed as $D^* = RA^{1/2}/\left(2eI_{dark}\right)^{1/2}$.[38] *D** reaches its maximum value of 8.2×10^{12} Jones at a fixed gate value of 12 V (insert of **Figure 2**d), where a much smaller dark current and a relatively large photocurrent contribute together to this result. The response time is another vital factor for high-speed phototransistor.[43] It is clear that the devices have almost the same "on" and "off" current during seven cycles. No obvious degradation is found as illustrated in Figure S4 Supporting Information, implying the great stability. The rise time of the detector is reasonably fast ~ 32 μs, with a decay time of ~ 98 μs, as shown in **Figure 2**e, which is one of the fastest values among reported Bi_2O_2Se phototransistors. The decay time of the photocurrent is dominated by a fast component of ~ 20 μs and a slow component of ~ 78μs, indicating the existence of multiple mechanism for recombination.[44] The fast decay time accounts for the direct recombination of electron and hole in bandgap,[45] while the multiple trap states, i.e., disorder or defects, and oxide charge[46] in Bi_2O_2Se or Bi_2O_2Se-Al_2O_3 interface are responsible for the slow release time. Then, we also verify the response time by ascertaining the -3 dB bandwidth of Bi_2O_2Se phototransistors in **Figure 2**f. The decrease in the amplitude of the photocurrent is measured by modulating the incident light signal with increased frequency using an optical chopper wheel. The photocurrent signals are normalized to the maximum at

low modulation frequencies. With the increasing modulation frequency, the normalized signal begins to reduce. The -3 dB bandwidth is a common figure of merit of phototransistors, where the signal drops to 70% of its initial value,[47] which for our devices are 5.4 kHz (V_G = -12 V) and 1.5 kHz (V_G = 0 V). From this we can extract a rise time using $\tau_{rise} \approx 0.35/f_{-3dB}$ about 59 μs, which is in good agreement with the data extracted from **Figure 2**e (~ 32 μs).

In order to further analyze quantitatively the response time dependence of top-gate voltage, the decay time of phototransistor is extracted as indicated in **Figure 3**a. The decay time of top-gate phototransistor increase from 98 μs to 4.4 ms, corresponding to V_G changing from -12 V to 12 V. To further explore the mechanisms of the decay time, band diagrams of the device under voltage operation are illustrated in **Figure 3**b and **3**c. The right side of the *y*-axis shows a band diagrams with dispersed gap-states to simplify the carrier dynamics, while the left side demonstrates a more concrete, continuous energy distribution of the density of states (DOS).[46] There are multiple trap states and combinations due to disorder, defects, or oxide charge at the surface of Bi_2O_2Se or at the interface of Bi_2O_2Se and Al_2O_3. In order to understand the mechanism behind the phenomenon, we should distinguish recombination centers and trap states.[45] The recombination center is located at midgap (x in **Figure 3**b and **3**c), which promotes electron-hole pairs recombination. However, the trap states only trap one type of photocarriers (electrons or holes), leaving the other photocarriers free and circulating with prolonged life time (τ_{trap}). With external source-drain bias, these free photocarriers transfer time is called $\tau_{transit}$. For $V_G > V_{Th}$ (threshold voltage) in **Figure**

3b, the Fermi level E_{F0} is located close to the conduction band and the majority of available electron trap states are filled, only leaving few recombination centers. Under low power intensity, the lowest-lying, long-lived traps filled first.[44,46] Under this case, there are few recombination centers and the detrapping process needs a long time, [36] thus a long decay time is acquired in **Figure 3**a. Moreover, high photoconductive gain ($G = \tau_{trap}/\tau_{transit}$) is acquired, which accounts for high responsivity in **Figure 2**c. As power increasing, more photocarriers are excited, but relatively less photocarriers can be trapped, giving rise to lower responsivity as illustrated in **Figure 2**c.[36] At $V_G < V_{Th}$, the Fermi level E_{F0} moves away from the conduction band, only few trap states are occupied. More states above E_{F0} are unoccupied, which can serve as recombination centers, favoring electron-hole pairs recombinationn.[48] In this case, the decay time decrease in **Figure 3**a.

In order to quantify the photosensitivity of 2D Bi$_2$O$_2$Se devices, we summarize the responsivities for 360 nm, 405 nm, 532 nm, 808 nm ,1310 nm and 1550 nm illumination as scatter plotted in **Figure 4**a. This outstanding performance can be further evidenced by high sensitivities along the whole spectrum from ultraviolet to telecom band (300 nm~1800 nm), such as 108696 A/W at 360 nm, 50055 A/W at 405 nm, 25505 A/W at 532 nm (Figure S5, Supporting Information), 843.5 A/W at 808 nm 118 A/W at 1310 nm and 22.12 A/W at 1550 nm, respectively. The responsivities are consistent with the absorption trend, reaching to the highest value at UV band? As shown in **Figure 4**b. Further, the calculated photoresponsivity as a function of incident laser power and gate voltage illuminated at 360 nm is presented in 2D map in

Figure 4c. Maximum responsivity reaches to 108696 A/W at low power intensity (0.23 nW) and large positive voltage, due to the lower contact resistance at the large gate voltage regime where the Bi_2O_2Se is electrically doped.[45] Moreover, the rise and decay time is about 32 ms and 101 ms at 360 nm, respectively (Figure S6, Supporting Information), because high photon energy can excite more deep impurities to conduction band, leading to slow response time.[49] The response speed of Bi_2O_2Se phototransistors is slow not only in the ultraviolet band but also in the infrared band. **Figure 4**d shows the temporal response of Bi_2O_2Se phototransistor at 1550 nm, where the rise and decay time is about 44 ms and 181 ms, respectively, which account for photothermal effect at near infrared wavelength, because Bi_2O_2Se is a kind of thermoelectric materials with Seebeck coefficient of $\sim$ -100 μV/K,[50,51] which will be discussed in detail later.

To further verify the photocurrent generation mechanism in the Bi_2O_2Se phototransistors, high-resolution spatial photocurrent mapping is carried out under a confocal optical microscope (see the Experimental Section for details). The modulated photocurrent signals are amplified and detected using the lock-in amplifier. From the photocurrent mapping diagram, it can be concluded that the photovoltaic and photogating effects are dominated in the photocurrent generation mechanism. The optical microscopy image of the device is described in Figure S6 Supporting Information, in which the right electrode is defined as drain (D) and the left electrode is source (S). Upon 940 nm illumination, the photocurrent is generated at the electrode contact edge without bias as shown in **Figure 5**a (the red region implies a

negative photocurrent generation, while the bright yellow region denotes positive photocurrent generation), which are influenced significantly by the Schottky barrier at the interface between metal and semiconductor, where electron-hole pairs are excited through absorbing light and laterally separated by built in potential resulting in the generation of photocurrent at opposite directions. The corresponding schematic is presented in **Figure 5**h, the width of depletion region consisting of two parts: W_s and W_D. The width of W_D is larger than W_s, owing to the Schottky barrier height in the D side higher than S side, corresponding to **Figure 5**a. Under this circumstance, the photothermal effect may also affect the photocurrent generation mechanism, only accounting for small proportion. Owing to the fact that Bi_2O_2Se is thermoelectric material with the Seebeck coefficient of ~ -100 µV/K,[50] there is a significant difference between Seebeck coefficients of Bi_2O_2Se nanosheets and the Au electrodes.[51] Under illumination, the local absorption of the laser creates a local heating of the junction between the gold electrode and Bi_2O_2Se nanosheets (ΔT). This local heating of the junction is translated into a voltage difference (ΔV_{PTE}), which will drive current through the device, leading to the photothermal effect. Moreover, the Schottky barrier height between D-Bi_2O_2Se and S-Bi_2O_2Se side can be effectively modulated by applied source-drain bias. When V_{ds} = 1 mV, the band slope between S and Bi_2O_2Se interface increases and the depletion region (W_s) extends further, which accelerates the electrons and holes separation (**Figure 5**i), leading to the enhancement of photocurrent at S side in **Figure 5**b. When exchanging the direction of V_{ds} bias (V_{ds} = -1 mV), the band slope of S-Bi_2O_2Se can be lower than that

D-Bi_2O_2Se side as described in **Figure 5**j, therefore, inverting the band slope and enhancing the photocurrent at D side (**Figure 5**c). The penetration of depletion into channel is enlarged with increasing Schottky barrier height when V_{ds} bias increase as described in **Figure 5**k and l, where electrons and holes photogenerated in depletion region drift quickly and separation by local electronic field, reducing the rate of combination and thus increasing the photocurrent. In this case, the photogating effect also play a vital role. Few electrons are trapped accounting for photoconductive gain, so the channel is all bright as described in **Figure 5**d and e. Moreover, with increasing the V_{ds} bias to ±1 V, there are also two depletion regions consisting of W_s and W_D (**Figure 5**m and n). The depletion region with the ohmic-like contact (reverse biased Schottky barrier) can be narrow enough such that voltage drop associated with charge trap states become important.[52] What's more, with the increase of the V_{ds} bias, the photogating effect is further enhanced when the majority of available electron trap states are filled. Thus, the strong photocurrent generates through the entire channel and is more pronounced on the side where the Schottky barrier is high as described in **Figure 5**f and g.

Highly sensitive phototransistors based on 2D Bi_2O_2Se nanosheets are promising for high-quality imaging application. **Figure 6**a describes the setup of the single-pixel imaging technique. The imaging target is a patterned light source, and the phototransistor is fixed in a camera dark box put on a two-dimensional rotary table. The imaging target is captured by the camera lens and focuses on the phototransistor. The phototransistor scans the target line by line, through controlling the movement of

the two-dimensional rotary table.[53] Then, the excellent properties of Bi_2O_2Se phototransistors can give rise to imaging with high-resolution and high-contrast to distinguish different parts, which is recorded by computer. In the ultraviolet region, the printed image "Nanjing University" (in Chinese) is used as an imaging target and a commercial ultraviolet flood light source (360 nm, 15 W) is placed behind it. The Bi_2O_2Se device is configured as a point-like detector to collect the reflected light and a 500 X 500 pixels image is obtained with good contrast (in **Figure 6**b). Moreover, a visible image "NJU" is acquired in Figure S8 (Supporting Information), by replacing the ultraviolet source with white CCD light source, measuring at the same case. At the infrared wavelength, the 1000℃, blackbody-like, radiant heated tube is selected as the infrared target, and a 780 nm high-pass filter is placed in front of the detector. In this case, the U-shaped tube image is acquired in Figure S9 (Supporting Information). Moreover, the characterization of the photoresponse for the same Bi_2O_2Se phototransistor at 1,310 nm demonstrates that the device has excellent long-term stability as shown by **Figure 6**c. There is no obvious difference in photoresponse between the as-fabricated and after two months, which is vital for practical applications.

To compare the phototransistor performance based on the Bi_2O_2Se with other 2D semiconductors prepared by CVD or mechanical exfoliation (ME) methods, the photoresponsivity (*R*), external quantum efficiency (*EQE*), specific detectivity (*D**) and rise time (τ_{rise}) are summarized in **Table 1**. It is noted that Bi_2O_2Se phototransistors show excellent performance in photoresponsivity and external

quantum efficiency, both of which are among the highest values in phototransistors based on 2D semiconductors.[11,33,54-56] In terms of response time, SnS_2 exhibits fast respond time ($\sim 5 \times 10^{-3}$ ms),[38] but it is limited by their low photoresponsivity (8.8×10^{-3} A/W)，low external quantum efficiency (2.4 %) and narrow band photodetection range (457 nm). InSe phototransistors with a broad response range from visible to near-infrared region (450-785 nm).[11] However, it shows much lower photoresponsivity (12.3 A/W) and external quantum efficiency (1367 %), which are four orders magnitude smaller than our results (1.09×10^5 A/W and 1.5×10^7 %). In_2Se_3[33] and ReS_2[37] based phototransistors all describe high detectivity (4.4×10^7 Jones, 2.3×10^{12} Jones) capability, while slow response time (2 ms, 18 ms) and low photoresponsivity (1.21×10^3 A/W, 3.95×10^2 A/W) limit its applications. These results clearly suggest that Bi_2O_2Se is one of the most promising materials for high-performance photoelectronic applications.

3. Conclusions

In conclusion, we have exquisitely designed Bi_2O_2Se phototransistors using high-quality large area ($\sim$180 μm) Bi_2O_2Se nanosheets grown by a modified CVD method. The photodetection wavelength of the device covers UV-Vis-NIR (360 $\sim$1800 nm) range and the photoresponsivity reaches up to 108696 A/W at 360 nm (the highest value reported to date), 50055 A/W at 405 nm, 25505 A/W at 532 nm，843.5 A/W at 808 nm, 118 A/W at 1310 nm and 22.12 A/W at 1550 nm, respectively. Upon 405 nm illumination, the *EQE* approaches up to 1.5×10^7 %, which is a record among currently reported 2D semiconductors and approximately two orders of magnitude higher than other CVD-grown 2D semiconductors. These outstanding properties can

WILEY-VCH

be explained by photogating, photovoltaic and photothermal effects. With such excellent optoelectronic merit, we envision that the Bi_2O_2Se nanosheets will become not only a valuable candidate to construct advanced appliances of optical sensing and low power consumption FETs but also an active component to fabricate integrated circuits.

4. Experimental Section

Growth and characterization of Bi_2O_2Se: The 2D material of Bi_2O_2Se is synthesized via the modified CVD method. Bi_2O_3 powder (purity 99.99%) and Bi_2Se_3 powder (purity 99.99%) are placed in the hot center inside the tube furnace and separated by 8 cm, respectively. Then the tube is sealed, evacuated to 30 Pa and flushed with high-purity Ar gas in the range of 100 ~ 150 sccm. The growth time is maintained for 30 ~ 90 minutes. With this approach, large-area (400 ~ 10000 μm^2), high crystalline Bi_2O_2Se nanosheets can be synthesized in temperature range of 550 °C~630 °C.

Transfer of Bi_2O_2Se onto Cu Grid and STEM Characterization: The TEM samples are prepared with a methacrylate (PMMA)-mediated transfer method, the as-synthesized samples are transferred onto the lacey carbon film supported copper grids for TEM characterization with the assistance of BOE solution. First, the mica substrates with the as-grown CVD samples are spin coated with PMMA at 2000 r.p.m. for 60 s. Afterward, PMMA-coated sample is peeled off by etching away the underneath mica substrate in BOE solution. Next, the floating PMMA film is transferred to the DI water and scooped up by a TEM Cu grid. Then, it merged into acetone for about 24 h to remove PMMA.

Device fabrication and measurements: The top-gate Bi_2O_2Se phototransistors with

30 nm Al_2O_3 as dielectric layer were fabricated through the transfer electronic method. The 30 nm Al_2O_3 is deposited by atomic layer deposition. Electrical measurements are carried out by the Keithley 2614B in a close-cycle cryogenic probe station with basepressure (10^{-6} Torr) at room temperature. For photoresponse characterization, we used 360, 405, 532, 808, 1310 and 1,550 nm laser diodes, respectively. The beam is guided through an optical fiber with a FC/PC ferrule and is subsequently incident onto the channel of the devices without focusing. The beam at the device is measured to be Gaussian-shaped with a diameter of about 400 μm. The photocurrent mapping is performed in air, by scanning over the device using Thorlabs GVS212, and modulated photocurrent signals are amplified and detected using the lock-in amplifier (Stanford SR830, Stanford Research Systems Inc.) technique. Photocurrent mapping is performed under 940 nm continuous laser illumination, which is modulated by a squarewave signal generator source.

Supporting Information

Supporting Information is available from the Wiley Online Library or from the author.

Acknowledgements

References

[1] X. Gong, M. H. Tong, Y. J. Xia, Y. J. Xia, W. Z. Cai, J. S. Moon, Y. Cao, G. Yu, C. L. Shieh, B. Nilsson, A. J. Heeger, *Science* **2009**, 325, 1665.

[2] S. Chen, C. J. Teng, M. Zhang, Y. R. Li, D. Xie, G. Q. Shi, *Adv. Mater*. **2016**, 28, 5969-5974.

[3] Y. Xie, B. Zhang, S. X. Wang, D. Wang, A. Z. Wang, Z .Y. Wang, H. H. Yu, H. J. Zhang, Y. X. Chen, M. W. Zhao, B. B. Huang, L. M. Mei, J. Y. Wang, *Adv. Mater*. **2017**, 29, 1605972.

[4] P. Avouris, *Nano Lett*. **2010**, 10, 4285-4294.

[5] F. Bonaccorso, Z. Sun, T. Hasan, A. C. Ferrari, *Nat. Photonics* **2010**, 4, 611.

[6] Q. H. Wang, K. Kalantar-Zadeh, A. Kis, J. N. Coleman, M. S. Strano, *Nat. Nanotechnol.* **2012**, 7, 699.

[7] O. Lopez-Sanchez, D. Lembke, M. Kayci, A. Radenovic, A. Kis, *Nat. Nanotechnol.* **2013**, 8, 497.

[8] A. Splendiani, L. Sun, Y. B. Zhang, T. S. Li, J. Kim, C. Y. Chim, G. Galli, F. Wang, *Nano Lett.* **2010**, 10, 1271.

[9] L. K. Li, Y. J. Yu, G. J.Ye, Q. Q. Ge, X. D. Ou, H. Wu, D. L. Feng, X. H. Chen, Y. B. Zhang, *Nat. Nanotechnol.* **2014**, 9, 372.

[10] F. N. Xia, H. Wang, Y. C. Jia, *Nat. Commun.* **2014**, 5, 4458.

[11] S. R. Tamalampudi, Y. Y. Lu, U. R. Kumar, R. Sankar, C. D. Liao, B. K. Moorthy, C. H. Cheng, F. C. Chou, Y. T. Chen, *Nano Lett.* **2014**, 14, 2800-2806.

[12] X. S. Li, W. W. Cai, J. An, S. Y. Kim, J. Nah, D. X. Yang, R. Piner, V. Aruna, I. Jung, E. Tutuc, S. K. Banerjee, L. Colombo, R. S. Ruoff, *Science*, **2009**, 324, 1312.

[13] L. W. Zhang, S. L. Shen, M. Li, L. Y. Li, J. B. Zhang, L. W. Fan, F. Cheng, C. Li，M. Zhu, Z. Kang, J.Sun, T.Y. Zhai, Y.H.Gao, *Adv.Optical Mater.* **2019**, 1801744.

[14] Y. X. Lin, Q. Ma, D. C. Shen, B. IIyas, Y. Q. Bie, A. Liao, E. Ergecen, B. N. Han, N. N. Mao, X. Zhang, X. Ji, Y. H. Zhang, J. H. Yin, S. X. Huang, M. Dresselhans, N. Gedik, P. Jarillo-Herrero, X. Li, J. Kong, T. Palacios, *Sci. Adv.* **2019**, 5, 1943.

[15] W. Choi, M. Y. Cho, A. Konar, J. H. Lee, G. Cha, S. C. Hoog, S. Kim, J. Kim, D. Jena, J. Joo, S. Kim, *Adv. Mater.* **2012**, 24, 5902.

[16] M. Q. Huang, M. L. Wang, C. Chen, Z. W. Ma, X. F. Li, J. B. Han, Y. Q. Wu, *Adv. Mater.* **2016**, 28, 3481-3485.

[17] M. J. Li, C. Y. Lin, S. H. Yang, Y. M. Chang, J. K. Chang, F. S. Yang, C. R. Zhong, W. B. Jian, C. H. Lien, C. H. Ho, H. J. Liu, R. Huang, W. W. Li, Y. F. Lin, J. H. Chu, *Adv. Mater.* **2013**, 25, 5714.

[18] H. J. Zhang, C. X. Liu, X. L. Qi, X. Dai, Z. Fang, S. C. Zhang, *Nat. Phys.* **2018**, 1803690.

[19] J. X. Wu, H. T. Yuan, M. M. Meng, C. Chen, Y. Sun, Z. Y. Chen, W. H. Dang, C. W. Tan, Y. J. Liu, J. B. Yin, Y. B.Zhou, S. Y. Huang, H. Q. Xu, Y. Cui, H. Y. Hwang, Z. F. Zhong, Y. L. Chen, B. H. Yan, H. L. Peng, *Nat. Nanotechnol.* **2017**, 12, 530.

[20] J. Li, Z. X. Wang, Y. Wen, J. W. Chu, L. Yin, R. Q. Cheng, L. Lei, P. He, C. Jiang, L. P. Feng, J. He *Adv. Funct. Mater.* **2018**, 28, 1706437.

[21] J. X. Wu, Y. J. Liu, Z. Tan, C. W. Tan, J. B. Yin, T. T. Li, T. Tu, H. L. Peng, *Adv. Mater.* **2017**, 29, 1704060.

[22] Z. Y. Zhang, T. R. Li, Y. J. Wu, Y. J. Jia, C. W. Tan, X. T. Xu, G. R. Wang, J. Lv, W. Zhang, Y. H. He, L. P. Shi, H. L. Peng, H. L. Li, *Adv. Mater.* **2018**, 1805769.

[23] M. Meng, S. Y. Huang, C. W. Tan, J. X. Wu, Y. M. Jing, H. L. Peng, H. Q. Xu, *Nanoscale* **2018**, 10, 2704-2710

[24] C. Chen, M. X. Wang, J. W. Wu, H. X. Fu, H. F. Yang, Z. Tian, T. Tu, H. Peng, Y. Sun, X. Xu, J. Jiang, N. B. M. Schroter, Y. W. Li, D. Pei, S. Liu, S. A. Ekahana, H. T. Yuan, J. M. Xue, G. Li, J. F. Jia, Z. K. Liu, B. H. Yan, H. L. Peng, Y. L. Chen, *Science advances*, **2018**, 4, eaat8355.

[25] Y. Zhang, J. W. Chu, L. Yin, T. A. Shifa, Z. Z. Cheng, R. Q. Cheng, F. Wang, X. Y. Zhou, Z. X. Wang, J. He, *Adv. Mater*. **2019**,1900056.

[26] F. F. Cui, C. Wang, X. B. Li, G. Wang, K. Q. Liu, Z. Yang, Q. L. Feng, X. Liang, Z. Y. Zhang, S. Z. Liu, Z. B. Lei, Z. H. Liu, H. Xu, J. Zhang, *Adv. Mater*. **2016**, 28, 5019.

[27] J. X. Wu, C. W. Tan, Z. J. Tan, Y. J. Liu, J. B. Yin, W. H. Dang, M. Z. Wang, H. L. Peng, *Nano Lett.* **2017**, 17, 3021.

[28] J. X. Wu, C. G. Qiu, H. X. Fu, S. L. Chen, C. C. Zhang, Z. P. Dou, C. W. Tan, T. Tu, T. R. Li, Y. C. Zhang, Z. Y. Zhang, L. M. Peng, P. Gao, B. H. Yan, H. L. Peng, *Nano lett.* **2018**.

[29] Y. H. Lee, X. Q. Zhang, W. J. Zhang, M. T. Chang, C. T. Lin, K. D. Chang, Y. C. Yu, J. T. W. Wang, C. S. Chang, L. J. Li, *Adv. Mater.* **2012**, 24, 2320.

[30] K. K. Liu, W. J. Zhang, Y. H. Lee, Y. C. Lin, M. T. Chang, C. Y. Su, C. S. Chang, H. Li, Y. M. Shi, H. Zhang, C. S. Lai, L. J. Li, *Nano Lett*. **2012**, 12, 1538.

[31] A. Reina, X. T. Jia, J. Ho, D. Nezich, H. Son, V. Bulovic, M. S. Dreeselhaus, J. Kong, *Nano Lett.* **2009**, 9, 30.

[32] D. S. Tsai, K. K. Liu, D. H. Lien, M. L. Tsai, C. F. Kang, C. A. Lin, L. J. Li, J. H. He, *Acs Nano* **2013**, 7, 3905.

[33] R. B. Jacobs-Gedrim, M. Shanmugam, N. Jain, C. A. Durcan, M. T. Murphy, T. M. Murray, R. J. Matyi, R. L. Moore, B. Yu, *Acs Nano* **2014**, 8, 514.

[34] M. S. Long, E. F. Liu, P. Wang, A. Y. Gao, H. Xia, W. Luo, B. G. Wang, J. W. Zeng, Y. J. Fu, K. Xu, W. Zhou, Y. Y. Lv, S. H. Yao, M. H. Lu, Y. F. Chen, Z. H. Ni, Y. M. You, X. A. Zhang, S. Q. Qin, Y. Shi, W. D. Hu, D. Y. Xing, F. Miao, *Nano Lett.* **2016**, 16, 2254.

[35] O. L. Sanchez, D. Lembke, M. Kayci, A. Radenovic, A. Kis, *Nat. Nanotechnol.* **2013**, 8, 497.

[36] J. B. Yin, Z. J. Tan, H. Hong, J. X.Wu, H. T. Yuan, Y. J. Liu, C. Chen, C. W. Tan, F. R. Yao, T. R. Li, Y. L. Chen, Z. F. Liu, K. H. Liu, H. L. Peng, *Nat. Commun.* **2018**, 9,1

[37] E. Z. Zhang, Y. B. Jin, X. Yuan, W. Y. Wang, C. Zhang, L. Tang, S. S. Liu, P. Zhou, W. D. Hu, F. X. Xiu, *Adv. Funct. Mater.* **2015**, 25, 4076.

[38] G. X. Su, V. G. Hadjiev, P. E. Loya, J. Zhang, S. D. Lei, S. Maharjan, P. Dong, P. M. Ajayan, J. Lou, H. L. Peng, *Nano Lett.* **2015**, 15, 506.

[39] J. O. Island. S. I. Blanter, H. S. J. van der Zant, A. Castellanos,-Gomez, *Nano Lett.* **2015**, 15, 7853.

[40] F. C. Liu, S. J. Zheng, X. X. He, A. Chaturvedi, J. F. He, W. L. Chow, T. R. Mion, X. L. Wang, J. D. Zhou, Q. D. Fu, H. J. Fan, B. K. Tay, L. Song, R. H. He, C. Kloc, P. M.Ajayan, Z. Liu, *Adv. Funct. Mater.* **2016**, 26, 1146.

[41] B. J. Zheng, Y. F. Chen, Z. G. Wang, F. Qi, Z. S. Huang, X. Hao, P. J. Li, W. L. Zhang, Y. R. Li, *2D Mater.* **2016**, 3, 035024.

[42] Z. J. Li, H. Qiao, Z. N. Guo, X. H. Ren, Z. Y. Huang, X. Qi, S. C. Dhanabalan, J. S. Ponraj, D. Zhang, J. Q. Li, J. L. Zhao, J. X. Zhong, H. Zhang. *Adv. Funct. Mater.* **2018** 28, 1705237.

[43] X. Zhou, L. Gan, W. M. Tian, Q. Zhang, S. Y. Jin, H. Q. Li, Y. S. Bando, D. Golberg, T. Y. Zhai, *Adv. Mater.* **2015**, 27, 8035.

[44] L. Liu, F. Wang, B. Wu, N. Mu, W. Huang, H. L. Wang, C. H. Jin, L. Zhang, J. He, L. Fu, Y. Q. Liu, *Adv. Mater.* **2017**, 29, 1700439.

[45] K. Xu, Z. X. Wang, F. Wang, Y. Huang, F. M. Wang, L. Yin, C. Jiang, J. He, *Adv. Mater.* **2015**, 27,7881-7885.

[46] D. Kufer, G. Konstantatos, *Nano Lett.* **2015**, 15, 7307.

[47] J. D. Mehew, S. Unal, E. T. Alonso, G. F. Jone, S. F. Ramahan, M. F. Cracium, S. Russo, *Adv. Mater.* **2017**,1700222.

[48]. F. Guo, B. Yang, Y. B. Yuan, Z. G. Xiao, Q. F. Dong. Y. Bi, J. S. Huang, *Nat. Nanotechnol.* **2012**, 7, 798.

[49] Y. J. Dai, C. S. Wu, Z. Y. Wu, Z. H. Zhao, L. Li, Y. Lu, Z. L. Wang, *Adv. Sci.* **2019**,1900314.

[50] J. B. Yu, Q. Sun, *Appl. Phys. Lett.* **2018**, 112, 053901.

[51] K. Y. Zhang, C. G. Hu, X. L. Kang, S. X. Wang. Y. Xi, H. Lin, *Mater. Research Bulletin*, **2013**, 48, 3968-3972.

[52] W. J. Yu, Y. Liu, H. L. Zhou, A. X. Yin, Z. Li, Y. Huang, X. F. Duan, *Nat. Nanotechnol.* **2013**, 8, 952.

[53] X. D. Wang, H. Shen, Y. Chen, G. J. Wu, P. Wang, H. Xia, T, Lin, P. Zhou, W. D. Hu, X. J. Meng, J. H. Chu, J. L. Wang, *Adv. Sci.* **2019**,1901050.

[54] Q. D. Fu, C. Zhu, X. X. Zhao, X. L. Wang, A. Chaturvedi, C. Zhu, X. W. Wang, Q. S. Zeng, J. D. Zhou, F. C. Liu, B. K. Tay, H. Zhang, S. J. Pennycook, Z. Liu, *Adv. Mater.* **2018**, 1804945

[55] U. Khan, Y. T. Luo, L. Tang, C. J. Teng, J. M. Liu, B. L. Liu, H. M. Cheng, *Adv. Funct. Mater.* **2019**, 26, 1807979

[56] C. W. Tan, M. Tang, J. X. Wu, Y. N. Liu, T. R. Li, Y. Liang, B. Deng, Z. J. Tan, T. Tu, Y. C. Zhang, C. Liu, J. H. Chen, Y. Wang, H. L. Peng, *Nano Lett.* **2019**, 19, 2148-2153.
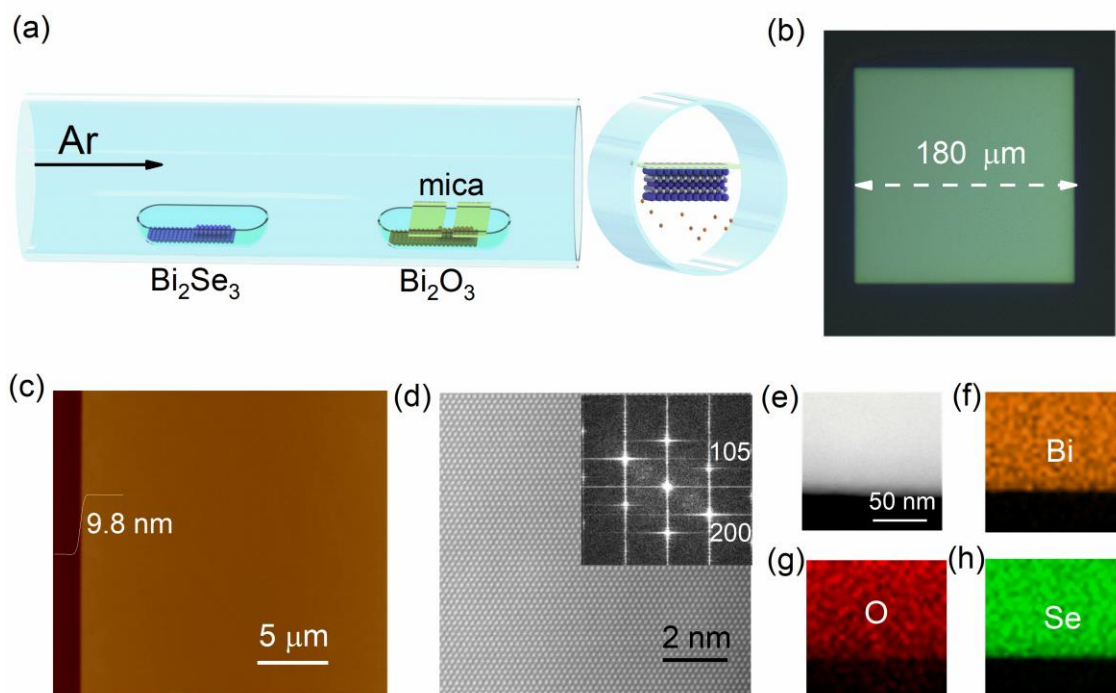
Figure 1. CVD Synthesis and characterization of Bi$_2$O$_2$Se. a) Schematic illustration of a modified CVD method to synthesize Bi$_2$O$_2$Se nanosheets on mica with the coevaporation sources of Bi$_2$Se$_3$ and Bi$_2$O$_3$. The mica was placed downwards, facing directly to the Bi$_2$O$_3$ powder. b) Typical optical microscopy image of synthesized 2D Bi$_2$O$_2$Se nanosheets on mica. c) AFM topography of the as-grown Bi$_2$O$_2$Se. The thickness is around 9.8 nm. d) HAADF image of the Bi$_2$O$_2$Se nanosheets and the corresponding FFT described in the insert. e-h) HAADF image of a Bi$_2$O$_2$Se nanosheets. (e) and corresponding elemental maps for Bi (f), O (g) and Se (h).
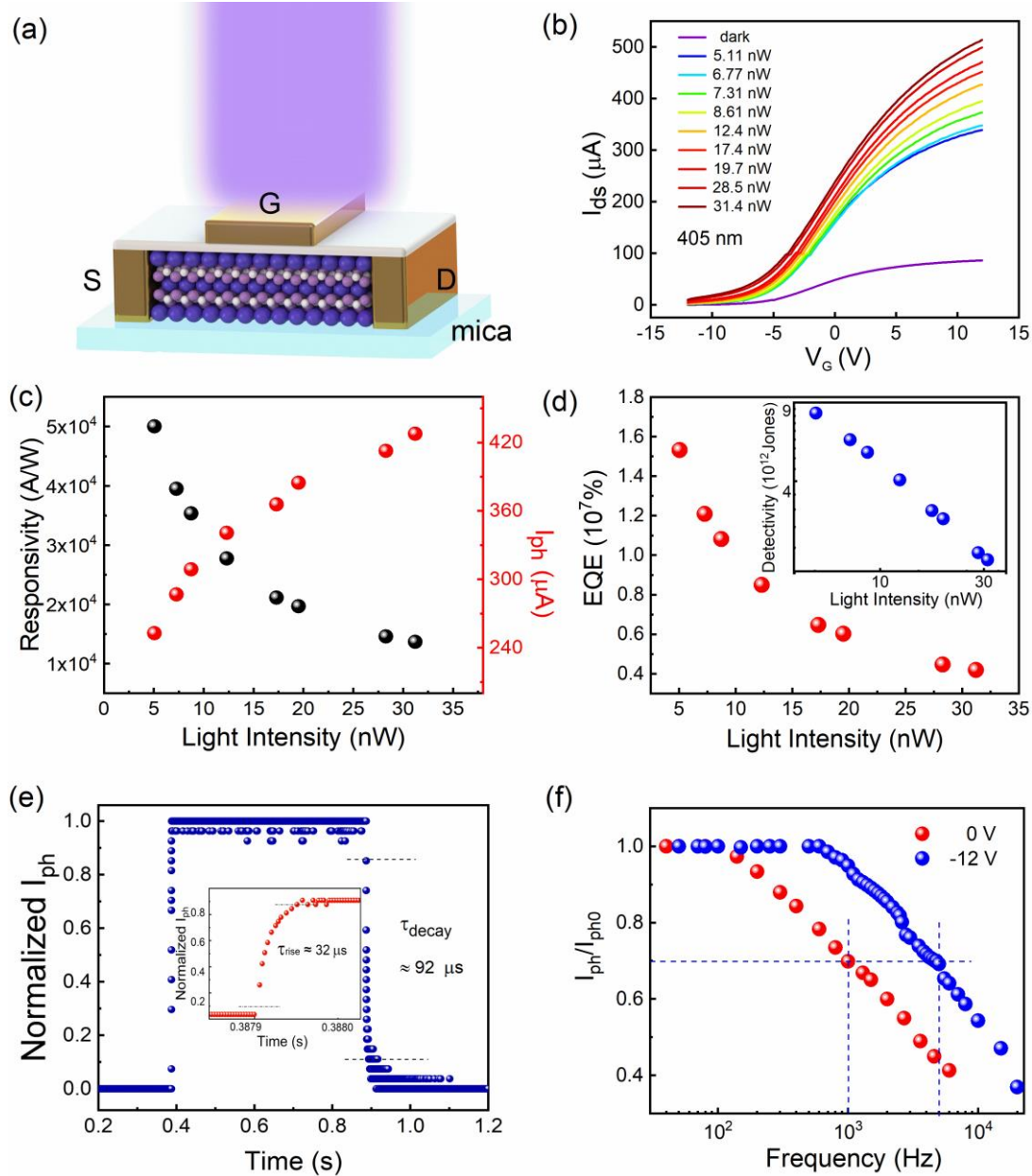
Figure 2. Optoelectronic characteristics of the top-gate Bi₂O₂Se phototransistors at the wavelength of 405 nm. a) Schematic of the top-gate Bi₂O₂Se phototransistor on mica. b) Top-gate transfer curves (I_{ds}-V_G) of the device with different light powers. c) Responsivity (left axis) and photocurrent (right axis) of the top-gate Bi₂O₂Se devices vs different optical illumination power density. d) *EQE* of the device under 405 nm laser illumination. Insert: the detectivity of the device. e) Time-resolved

photoresponse of the Bi_2O_2Se. Inset: the rising time is about 32 ms. f) Normalized

photoresponse as a function of light modulation frequency.

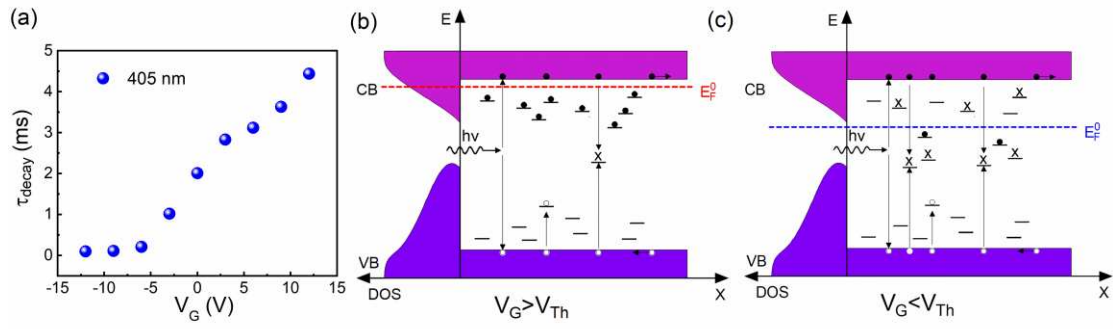**Figure 3. Tunable photoresponse of top-gate Bi₂O₂Se phototransistors.** a) Temporal response of phototransistors under different top-gate voltage. b-c) A schematic mechanism based on energy band is proposed to explain our observation.
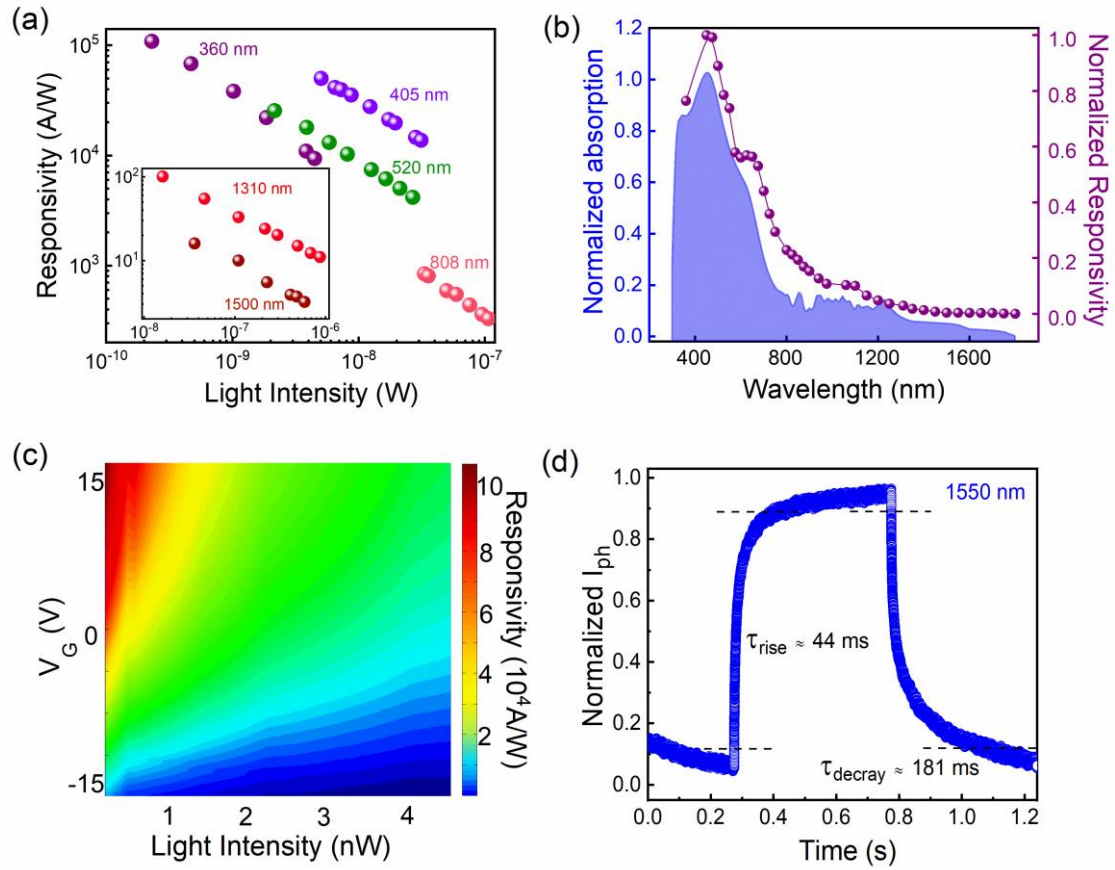
Figure 4. Optoelectronic response in a wide spectral range and carrier dynamics.

a) Responsivity as a function of the incident light power at wavelength of 360, 405，

532, 808, 1310 nm and 1550 nm (in the insert), respectively. b) Spectral responsivity

(left axis) from UV to telecom band of the top-gate Bi_2O_2Se device. Blue shaded

areas correspond to the absorption (right axis) of the device. c) Dependence of

photoresponsivity with different incident powers and gate voltage bias at wavelength

of 360 nm. d) Time-resolved photoresponse of the Bi_2O_2Se at 1550 nm.

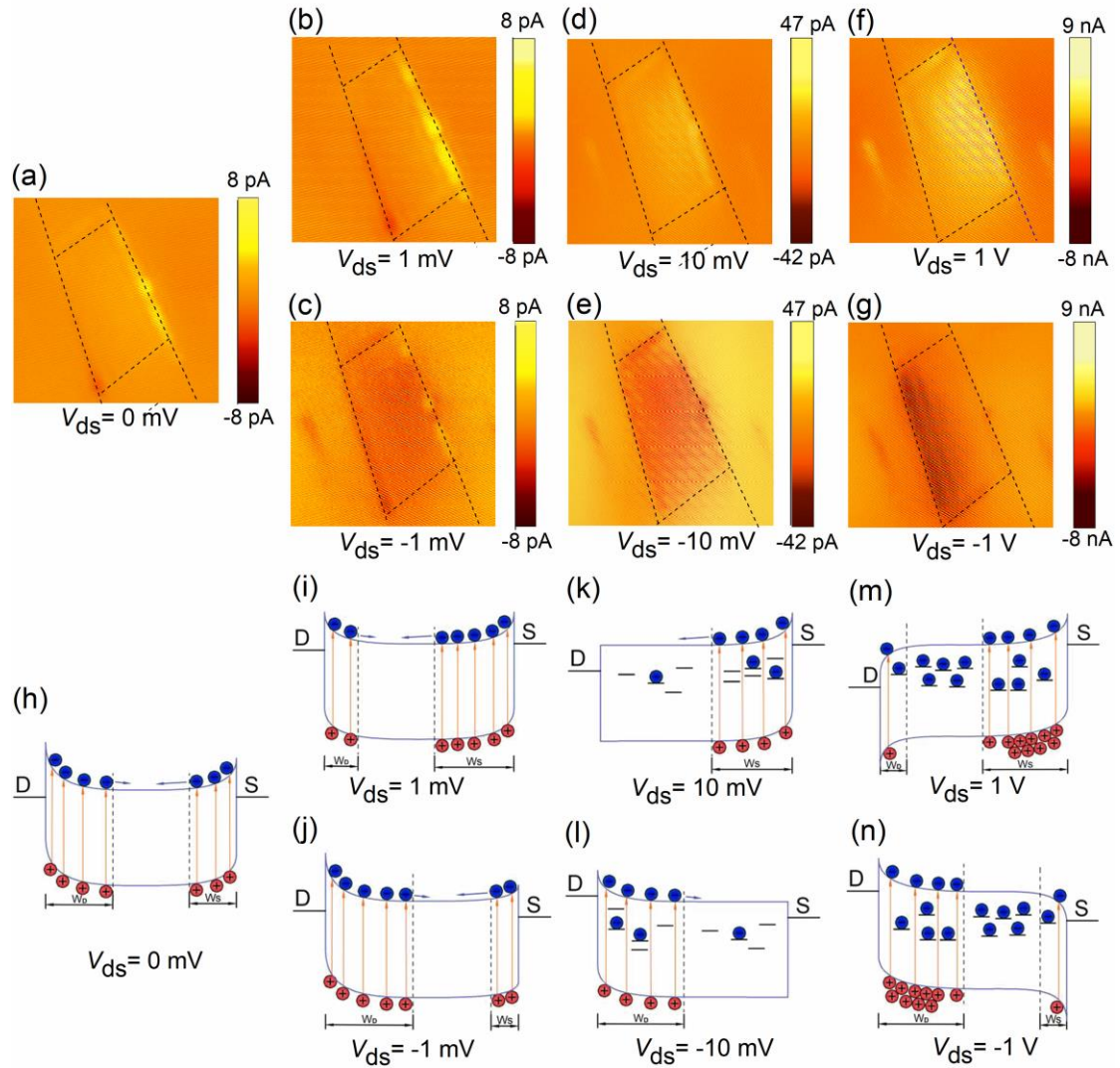**Figure 5. Photocurrent mapping under 940 nm illumination and energy-band diagrams.** a)-g) Photocurrent images of the Bi_2O_2Se device under 940 nm continuous laser illumination at different bias. The black line represents the device channel. h)-n) Energy-band diagrams of the semiconductor Bi_2O_2Se under the different bias.
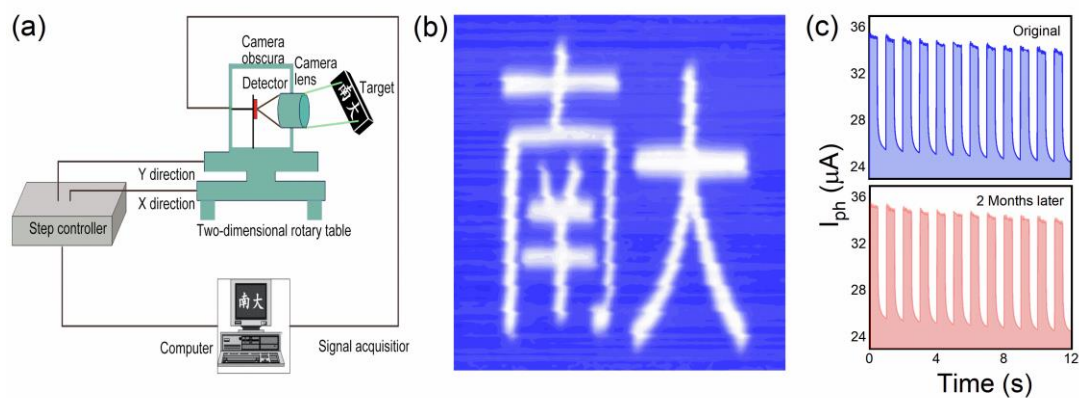
Figure 6. Imaging measurement in the ultraviolet wavelength and stability test. a) Single-pixel imaging configuration. b) Ultraviolet imaging "Nanjing university" (in Chinese) using the single-pixel imaging technique. c) The photoresponse of Bi_2O_2Se device in ambient as fabricated and after two months at the wavelength of 1310 nm.

Table 1. Comparison of phototransistor performances based on the Bi$_2$O$_2$Se with other 2D semiconductors prepared by CVD or mechanical exfoliation (ME) methods.

Materials	Method	Bandgap [eV]	Spectral range [nm]	Responsivity [A/W]	External quantum efficiency [%]	Detectivity [Jones]	Rise Time [ms]	Reference
ReS$_2$	ME	1.5	532	1.21×10^3	—	4.44×10^{10}	2	[37]
SnS$_2$	CVD	2.1	457	8.8×10^{-3}	2.4	2×10^9	5×10^{-3}	[38]
InSe	ME	1.3	450-785	12.3	1367	1.07×10^{11}	40	[11]
In$_2$Se$_3$	ME	1.3	300	3.95×10^2	1.63×10^5	2.26×10^{12}	18	[33]
Bi$_2$O$_2$Se	CVD	0.8	808	6.5	—	8.3×10^{11}	2.8	[20]
Bi$_2$O$_2$Se	CVD	0.8	532	2.2×10^4	—	3.4×10^{15}	6	[50]
Bi$_2$O$_2$Se	CVD	0.8	360-1800	1.09×10^5	1.5×10^7	8.2×10^{12}	0.032	This work

The table of contents entry

We synthesized high-quality large area Bi$_2$O$_2$Se nanosheets through the modified CVD method with the face-down approach. The photodetection wavelength of the device covers ultraviolet (UV)-visible (Vis)-near infrared (NIR) range and the photoresponsivity reaches up to 108696 A/W at 360 nm, which is a record among currently reported 2D semiconductors. Upon 405 nm illumination, the external quantum efficiency (*EQE*) approaches 1.5×10^7% and rising time achieves to 32 μs. The mechanism of the high responsivity in a wide spectral range (360 nm~1800 nm) has been explained by a combination of photogating, photovoltaic and photothermal effects.

Keyword: Bi$_2$O$_2$Se nanosheets; CVD growth; broadband phototransistors

Tong Tong, Yunfeng Chen, Shuchao Qin, Weisheng Li, Junran Zhang, Chunchen Zhang , Xiao Yuan, Xiaoqing Chen, Man Luo, Xinran Wang, Weida Hu*, Fengqiu Wang*, Wenqing Liu, Peng Wang, Xuefeng Wang*, Rong Zhang* and Yongbing Xu*

Title: Sensitive and UltraBroadband phototransistor Based on 2D Bi$_2$O$_2$Se Nanosheets with Spectral Response from 360 to 1800 nm

ToC figure: